Fermi surface and band structure of Ti₂SnC as observed by angle-resolved photoemission spectroscopy

Damir Pinek [1,*] Takahiro Ito [2,3] Kanji Furuta [3] Arnoldus J. van Bunningen [1,†] Patrick Le Fèvre,[4]
François Bertran,[4] and Thierry Ouisse[1,‡]

[1]*Université Grenoble Alpes, CNRS, Grenoble INP, LMGP, F-38000 Grenoble, France*
[2]*Synchrotron Radiation Research Center (NUSR), Nagoya University, Nagoya 464-8603, Japan*
[3]*Graduate School of Engineering, Nagoya University, Nagoya 464-8603, Japan*
[4]*Synchrotron SOLEIL, Saint-Aubin, Boîte Postale 48, F-91192 Gif-sur-Yvette Cedex, France*

We present an experimental study of the electronic states of the nanolamellar compound Ti₂SnC by means of angle-resolved photoemission spectroscopy (ARPES). Experiments were performed on macroscopic single crystals, and the observed Fermi surface and band structure were systematically compared with the output of density functional theory calculations. The fine details of the Fermi surface predicted by theory are duly evidenced by the ARPES measurements. The multiply connected Fermi surface (FS) is formed by a combination of quasi-two-dimensional corrugated tubes and quasi-one-dimensional thin plates, centered on high-symmetry axes and points, respectively. The quasi-one-dimensional FS region displays a clear Dirac-like dispersion. An evanescent surface state is observed in addition to the bulk bands.

I. INTRODUCTION

The $M_{n+1}AX_n$ nanolamellar carbides, also referred to as MAX phases, form a large group of materials that have attracted a lot of attention over the past two decades [1–3]. They possess an unusual combination of metallic- and ceramic-like properties, and they are also the precursors for MXenes [4,5], a class of bidimensional materials that show great promise for energy storage applications [6] and other fields [7].

Some bulk MAX phases such as Ti₂AlC, Ti₃SiC₂, or Cr₂AlC have been investigated extensively due to their potential for applications in extreme conditions [2]. In contrast, and as for many other compounds belonging to the MAX phase family [2,8], the properties of Ti₂SnC have been the focus of a relatively small number of studies (see, e.g., [9–17]). Yet this compound exhibits remarkable crack healing capabilities [9], which could lead to the development of ceramic materials with a prolonged lifetime under harsh thermal conditions [9,10].

Up to now, Ti₂SnC has been synthesized under polycrystalline powder form through standard sintering methods [11–14], as well as in the form of polycrystalline thin film by means of chemical or physical deposition techniques [15]. The electronic properties of Ti₂SnC are similar to those of most MAX phases, with an electronic conductivity higher than other Sn-based MAX phases [11,12]. The electronic structure of Ti₂SnC is reported in several computational studies [16,17], but the latter lack a precise determination of both the band structure (BS) and the Fermi surface (FS), which were only computed on very coarse k-meshes [17]. To our knowledge, the electronic structure of Ti₂SnC has not been experimentally probed yet.

Recently, the Fermi surface and the near-Fermi-level band structure of Cr₂AlC, V₂AlC, and Ti₃SiC₂ were experimentally probed by means of angle-resolved photoemission spectroscopy (ARPES) and density functional theory (DFT) calculations [18–20]. Following these developments, it was demonstrated that rigid band models could describe the BS of the 211 MAX phases [21], a MAX phase's subclass to which Ti₂SnC belongs. Yet, its electronic band structure is expected to differ from its Al-based counterpart Ti₂AlC or other Al-based MAX phases [21]. As mentioned above, the BSs available in the literature were most often computed on very coarse k-meshes, which do not allow one to conduct a thorough and comprehensive analysis of the electronic structure.

The purpose of this work is to apply the methodology we used for other 211 MAX phases (and other similar compounds such as Mo₄Ce₄Al₇C₃ [22,23]) to Ti₂SnC: We combined ARPES experiments and DFT calculations in order to obtain a reliable description of the electronic states of Ti₂SnC near the Fermi level and at intermediate energies. As for Cr₂AlC and other phases, the specificity of our approach is that we grow macroscopic bulk single crystals of MAX phases for photoemission experiments. This paper details the growth of macroscopically large Ti₂SnC bulk single crystals. Their availability was key for probing the Ti₂SnC FS and BS through ARPES.

─────────

*Present address: European Synchrotron Radiation Facility (ESRF), CS 40220, F-38043 Grenoble Cedex 9, France; Corresponding author: damir.pinek@esrf.fr

†Present address: Condensed Matter and Interfaces, Debye Institute for Nanomaterials Science, Utrecht University, Princetonplein 1, 3584 CC Utrecht, The Netherlands.

‡Corresponding author: thierry.ouisse@grenoble-inp.fr

The FS of Ti$_2$SnC appears to be made up of a combination of nearly two-dimensional (2D) vertical tubes centered in Γ, and electron bands located around the H point (bands 43 and 44). The FS of the latter breaks down into two specific kinds of domains, one being 2D in-plane and the other 1D along c. The band structure and Fermi surface show some resemblance to Ti$_3$SiC$_2$ due to the predominance of the Ti d orbital contribution near E_F. Despite some slight discrepancies at intermediate energies, an overall good agreement between ARPES and DFT is found. An excellent agreement is obtained near the Fermi level. Evanescent surface states are spotted, and bulk linear dispersive features are observed and related to the complex morphology of bands 43 and 44 and their respective FSs and isoenergy surfaces. As for Ti$_3$SiC$_2$, these linear dispersions may lead to a non-negligible linear behavior of the magnetoresistance at a high magnetic field [20].

II. MATERIALS AND METHODS

Self-nucleated Ti$_2$SnC single crystals were synthesized by high-temperature solution growth in an induction-heated growth reactor, following a process similar to that detailed in [24–26]. The atomic ratio of Ti and Sn in the solution was around 1:1, and carbon was provided by the dissolution of the graphite crucible within the metallic solution. The high-temperature set point was between 1800 and 1850°C, imposed during 1 h before starting the slow cooling down (a few days). The lateral dimensions of the as-grown crystals are typically in the range of a few mm's, some of them reaching up to almost 1 cm. Crystals are up to a few 100 μm thick, and are oriented toward (0001). Single crystals were cut in 3 mm × 3 mm squares before being cleaved within the UHV chamber of the Cassiopée line at SOLEIL, which is equipped with a SCIENTA R4000 analyzer for ARPES experiments. Base pressure was set to about 10^{-9} Pa, and the temperature was set to 13.4 K. ARPES spectra were recorded with a photon energy of 97.5 eV in a linear horizontal polarization mode that is equivalent to the *s* pol configuration described in [18]. Figure 9(a) is an exception here as it was recorded for an energy of 22.5 eV at UVSOR-III BL7U. In this energy range, and for similar systems, k_z broadening is expected to be of the order of 0.25–1 Å^{-1} [27], suggesting that a nearly complete k_z averaging of the band will occur over the Ti$_2$SnC Brillouin zone (BZ), for which π/c is approximately 0.23 Å^{-1}. Energy resolution is of the order of 10 meV.

The angular window of the entry slit of the photoelectron detector goes from $-17.50°$ to 12.3°, with a resolution of 0.046° for the variable labeled as θ_x. One can define θ_x as the angle between the photoemitted electron beam line, which reaches the middle of the slit detector, and an electron beam line detected in another given part of the slit. θ_y is the angle between the same line defined by the emitted electron beam detected in the middle of the detector slit and the growth axis of the crystal. It evolves within the $[-10.75°, 32.75°]$ interval, varying with angular steps of 0.5°. As a short reminder, θ_x and θ_y define the value of k_x and k_y wave-vector coordinates in reciprocal space, and in this work the crystal was aligned so that k_x and k_y corresponded to the ΓK and ΓM crystal axes, respectively. The angle between the incoming light beam and

the mediator of the line of the slit detector was set to 45°. The overall experimental configuration is similar to the one used in [18], and a more detailed description of the experimental setup, including figures, can be found there. The ARPES analysis we performed is based on the framework of the three-step model [28]. Scattering of the outgoing electron when crossing the surface and other final-state effects are thus not taken into account.

All DFT calculations were performed with the full-potential LAPW+lo (linear augmented plane wave + localized orbitals) method implemented within the WIEN2K software [29]. The standard spinless Perdew-Burke-Ernzerhof (PBE) generalized gradient approximation (GGA) functional [30] was chosen. Wave functions were expanded up to an *RKM* cutoff parameter of 9 to guarantee that convergence was reached (*RKM* refers to the smallest "atomic sphere radius" *R* times the largest *K* vector of the LAPW expansion used). A dense $72 \times 72 \times 14$ Monkhorst-Pack cell was used. For GGA+SOC (spin-orbit coupling) calculations, the WIEN2K basis of relativistic orbitals was used to describe the Ti orbitals, and SOC was taken into account for all atoms. The overall level of convergence was set to 0.01 mRy. The Fermi surface plots and Fermi velocity maps were computed using FERMI SURFER and XCRYSDEN software [31,32].

III. FERMI SURFACE

As for other MAX phases, Ti$_2$SnC crystallizes in the $P6_3/mmc$ space group [2,33] [the associated unit cell is given in Fig. 1(a)] and its properties at the Fermi level E_F are mostly determined by the d orbitals of the Ti atoms [2,8]. In Fig. 1(c), the BS of Ti$_2$SnC is projected onto the various Ti d orbitals and Sn $p_x + p_y$ orbital states. Consistent with past density-of-states (DOS) calculations [17], the various Ti d orbitals dominate over other Sn p and other orbitals near E_F. Yet, about 1.5 eV below E_F, the Sn $p_x + p_y$ orbital contribution gets stronger, as expected from Sn orbital-projected DOSs [17], which are found to exhibit $5p$ local maxima around 2 and 3 eV. As for V$_2$AlC, Cr$_2$AlC, and Ti$_3$SiC$_2$, the knowledge of the orbital character of the bands is key to the understanding of the output of photoemission experiments [28,34], especially for the case of ARPES, where the experimental spectra are probed in a three-dimensional (E, θ_x, θ_y) or four-dimensional $(E, \theta_x, \theta_y, h\nu)$ parameter space.

Combined with the orbital and angular dependence of the photoionization cross section, orbital-projected BSs are used to assess which band can be observed for a given experimental configuration [28,34,35]. Here, the configuration is equivalent to the *s* pol mode described in [18] (note that in [18], the *x* and *y* axes are inverted with respect to the convention used here, and so are the roles of θ_x and θ_y). The angular dependence of the photoionization cross sections of the $3d$ orbitals was computed in [18] for Cr$_2$AlC from the formalism detailed in [36]. One would obtain similar curves for the $3d$ orbitals of Ti in Ti$_2$SnC. Accordingly, bands with a strong d_z^2 contribution at E_F should appear with a stronger intensity at small angle and decrease at higher angles [18]. Bands 41 and 42, which exhibit a non-negligible d_z^2 character at E_F [see Fig. 1(c)], should give a strong contribution to the FS spectra at small angle. As d_{yz} and d_{xz} contributions will overcome d_z^2 at larger
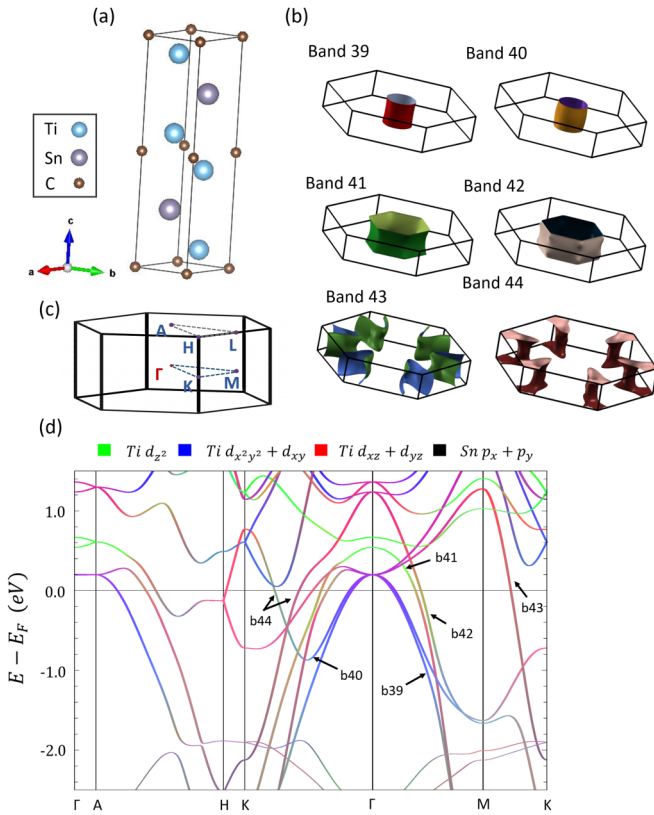
FIG. 1. (a) Ti$_2$SnC unit cell. (b) Fermi surfaces of Ti$_2$SnC plotted over the first BZ, for the four-hole bands (b39-42) and the two-electron bands crossing E_F (b43-44). (c) Sketch of the first Brillouin zone of Ti$_2$SnC, with indicated directions. (d) Ti$_2$SnC band structure projected onto Ti d orbitals, dominant at the Fermi level, and Sn $p_x + p_y$ orbitals.

angles, the contribution of the other bands will become more prominent at the edge of the first BZ and in the extended BZs. An asymmetry of the ARPES signal intensity should be observed over θ_x while the spectra should be symmetric along θ_y [18].

The ARPES Fermi surface map is shown in Fig. 2(a). The shape of the experimental FS spectra mostly corresponds to a projection of the DFT FS shown in Fig. 2(b). The DFT FS reproduces well the experimental spectra, but a few effects must be taken into account prior to other considerations: First, matrix element effects can be tackled by considering the angular dependence of the photoionization cross section mentioned above. Consistent with the analysis above, FSs of bands 41 and 42 appear prominently around the Γ point at (0.0 Å^{-1}, 0.0 Å^{-1}). For the Γ point located at $k_x = 0.0$ Å^{-1} and $k_y = 2.235$ Å^{-1} (corresponding to $\theta_x = -6.63°$ and $\theta_y = 26.5°$ before azimuth rotating and converting the experimental ARPES spectra into wave-vector units), the ARPES signal is less intense, and the FS tube associated with bands 39 and 40 can clearly be spotted. Secondly, the three-dimensional character of the FS needs to be considered. The Ti$_2$SnC Fermi surface involves four nearly 2D hole bands that form cylindrical, corrugated tubes (bands 39 and 40) and hexagon-shaped tubes (bands 41 and 42), with axes oriented along ΓA [see Fig. 1(c)]. These FSs form distinctive line patterns on the

ARPES spectra, almost not blurred due to their nearly 2D morphology. Hence, the effect of k_z broadening is expected to be negligible for these bands [37,38]. One must note that we hereby refer to k_z broadening as the fact that, for a given k_x, complete 3D bands contribute to the ARPES spectra, as they are spanned over a full Brillouin zone along k_z [37–40]. This broadening can thus be predicted by plotting a set of dispersion curves with k_z as a parameter that varies over one BZ, as shown in Figs. 6(a) and 7(a). We do neglect the final-state effects described in [20,41], which are also referred to as k_z broadening.

In contrast to the other bands, the contributions of bands 43 and 44 are electronlike. They exhibit well-defined interconnected domains that are either dispersive along k_z only (i.e., 1D-like; see the detailed discussion in Sec. IV B) or dispersive in-plane (i.e., 2D-like; see also Sec. IV B). While the FS of band 43 [Fig. 1(b)] is formed out of a warped tube centered on the KH axis (so that dispersion is rather 2D-like and in-plane), the band 44 FS consists in triangular, flat plates located within HLA planes (i.e., 1D-like with dispersion along c), and connected by tubes centered between the Γ and K points [i.e., 2D-like with in-plane dispersion; see Fig. 1(b)]. Signatures of these tubes are visible on the ARPES spectra, close to the coordinates (± 0.5 Å^{-1}, 1.5 Å^{-1}). Similar to band 50 of Ti$_3$SiC$_2$, the contribution of band 44 to Ti$_2$SnC ARPES spectra corresponds to an averaging of that FS over k_z [20]. Yet, due to the very small in-plane dispersion of this band in (k_x, k_y) near the H point, the k_z averaging should not lead to an intense "projected FS" pattern. This is consistent with the lower intensity of the H centered triangular surfaces displayed by the ARPES spectra [Fig. 2(a)].

The overall FS of Ti$_2$SnC thus shows a high degree of anisotropy, and a similar anisotropy is found for the Fermi velocity modulus map shown in Figs. 2(b) and 2(c). The morphology of the FS shows some similarity with Ti$_3$SiC$_2$ [20]. The Fermi velocity v_F, determined by using the FERMI SURFER software [31], appears to be minimum for the two embedded tubes closest to the ΓA axis. The Fermi velocity is maximum for band 43, over MK. Although all FS regions are highly anisotropic, their different orientations, combined with the high Fermi velocity values, in-plane or along k_z, suggest that transport in Ti$_2$SnC may not be nearly as 2D as a MAX phase such as Cr$_2$AlC [18]. In any case, it would be necessary to assess the anisotropy of the relaxation time in order to fully ascertain the anisotropies of Ti$_2$SnC transport coefficients [42,43], but this is way beyond the scope of this work. It is remarkable that the FS essentially consists of tubes and very thin plates, connected or not. This means that the electrons at the Fermi energy do not display 3D behavior. Some of them behave instead as if they were spatially confined in one dimension, with an energy dispersion restricted to the c axis (FS plates), whereas others are 2D, with an in-plane energy dispersion (tubelike FS parts with their axis directed along c). The 1D-like dispersion of band 44 is also very peculiar, for it corresponds to a 1D Dirac-like dispersion located in the H plane and slightly below E_F [see the two linear dispersions close to E_F along the HK axis in Fig. 1(c), joining at a 1D Dirac point located in H, whereas along AH and starting from H, the dispersion of the two bands is totally flat and degenerate, indicating a local 1D character]. The LAPW+lo approach
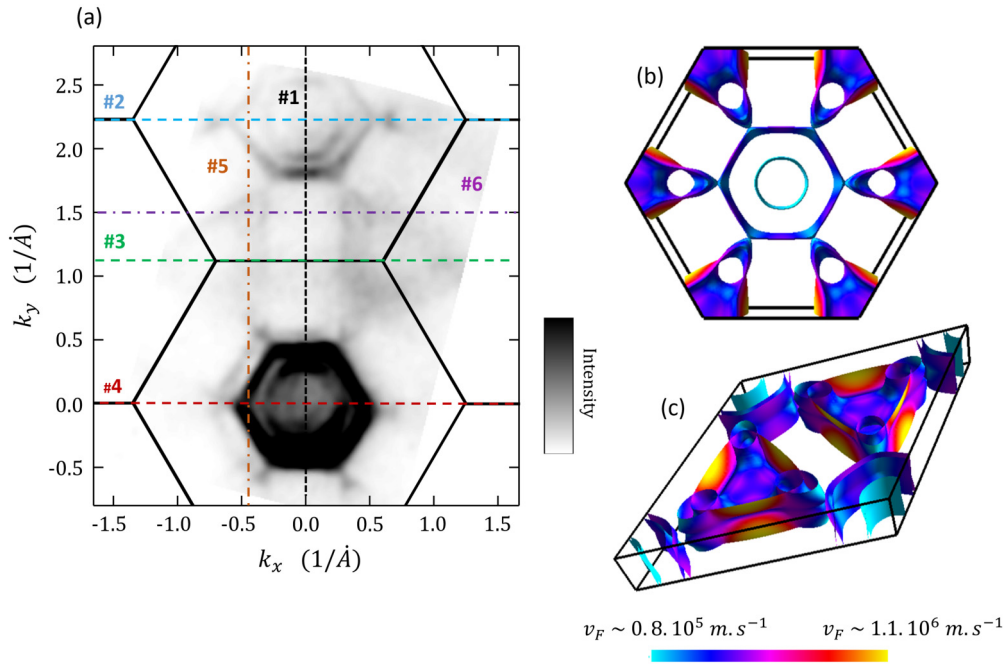
FIG. 2. (a) Extended ARPES Fermi surface mapping centered in Γ. The six directions indicated, respectively, correspond to the k_x axes for the BS in Figs. 5 (no. 1), 6(b) (no. 3), 7(b) and 7(c) (nos. 2 and 4), and 9(c) and 9(d) (nos. 5 and 6). For this intensity scale, the maximum of the ARPES signal is 471 and the minimum is 14. The Ti_2SnC FS computed by DFT is given within both the first BZ (b) and an alternative BZ centered in L (c), with the FS velocity moduli v_F represented as a color plot on the top of the surfaces.

makes it easy to determine how close the electron states are to a linear combination of atomic orbitals. Here, the output of the DFT calculations indicates that for electrons with an energy close to E_F, the weight of the augmented plane waves is small compared to that of the atomic orbitals. This justifies the discussion in terms of the orbital character of the bands. Ti atoms give the more prominent contribution to the states around E_F, as usually observed for MAX phases [2]. It is worth noting that the 1D region around the H point corresponds to Ti orbital contributions pointing out-of-plane, with an angle that allows Sn atom contributions to be associated with the electron wave functions with the wave vector around H (see Fig. 1), a feature needed for out-of-plane delocalization. In contrast, the Ti orbitals contributing to the in-plane hole bands which are centered in the Γ point are mostly restricted to the xy plane (see Fig. 1). A detailed experimental verification of those dispersions as well as a comparison between ARPES and DFT are presented in the next section.

IV. ENERGY BAND DISPERSION

A. General comparison between ARPES and DFT

Determination of the inner potential V_0 was estimated from the symmetry of band dispersive features along k_z at some k_x lines, though the interplane Fermi surface mostly consists of in-plane, quasi-two-dimensional regions. Figure 3(a) indicates which $k_\perp$ value is probed at a given $k_{//}$ for several photon energies $h\nu$. $h\nu = 97.5$ and 22.5 eV correspond to $k_\perp$ lying around Γ planes. Figure 3(b) shows interplane ARPES Fermi surface mapping of Ti_2SnC. ARPES trace lines nos. 7–9 defined in Fig. 3(a) result in the band structures shown in Figs. 3(c), 3(d), and 3(e) for $k_x = 0.65$ Å^{-1} (cut no. 7),

$k_x = 0.9$ Å^{-1} (cut no. 8), and $k_x = 1.35$ Å$^{-1} \approx$ KH (cut no. 9), respectively. The inner potential value was estimated around $V_0 = 22.5$ eV. The quality of raw ARPES data can be assessed by an examination of Fig. 4, which displays energy distribution curves (EDCs) and momentum distribution curves (MDCs). Figure 4 shows how clearly the band dispersions are observed along two high-symmetry directions.

Band-structure mappings over directions no. 1 (ΓM), no. 3 (MK), and the two equivalent nos. 2 and 4 (ΓK) directions, as defined in Fig. 2(a), are given in Figs. 5, 6, and 7, respectively. The prominent dispersive features in the 0 to -0.5 eV window show a high degree of consistency with DFT calculations. In Fig. 5, the bands along ΓM seem to delimitate well most of the dispersive features associated with each band. Nevertheless, the positions of several bands located at least 1 eV below E_F are slightly shifted compared to their expected position from DFT calculations. Most of these discrepancies appear within a restricted wave-vector range near the M point, starting from -1.0 eV below E_F and then following below. Bands 41 and 42 are very close to each other in that range, and both exhibit a minimum at the M point, located at -1.65 eV for the DFT bands. From DFT, and as highlighted in Figs. 5 and 6(a) for KMK, these bands are expected to depend weakly on k_z in this area, with an expected energy width of 20 meV for band 41 and 10 meV for band 42 when going from the M to the L point. Both bands would be degenerate at the edge of the BZ, along AL. The experimental ARPES spectra near the M point show very intense features, with an apparent width of around 0.5 eV at the M point. Overall, from -1 eV below E_F, the experimental k_z broadening seems to be somewhat larger than what was expected from the DFT predictions. This is also observed over MK as highlighted in Fig. 6(b). Broadening
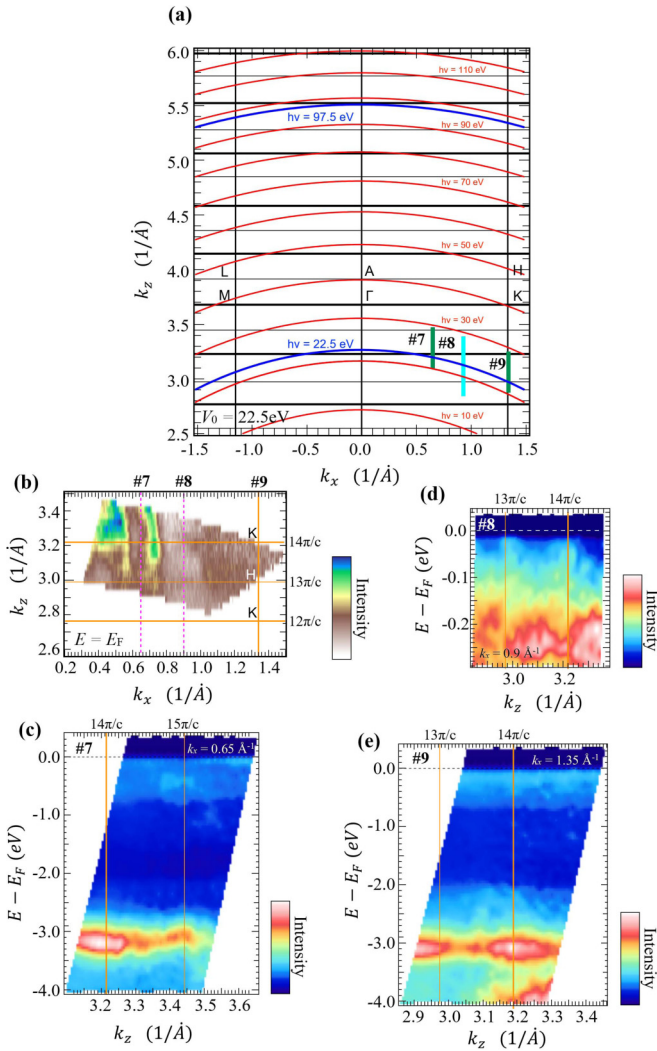
FIG. 3. Part (a) indicates which $k_\perp$ value is probed at a given $k_{//}$ for several $h\nu$'s. $h\nu = 97.5$ and 22.5 eV correspond to $k_\perp$ lying around Γ planes. (b) Interplane ARPES Fermi surface mapping of Ti$_2$SnC. ARPES trace lines nos. 7 and 8 in (c)–(e) are shown in (a) and (b). (c)–(e) Band structures along the cut no. 7 [(c) $k_x = 0.65$ Å^{-1}], no. 8 [(d) $k_x = 0.9$ Å^{-1}], and no. 9 [(e) $k_x = 1.35$ Å$^{-1} \sim$ KH], respectively.

FIG. 4. Raw ARPES spectra of Ti$_2$SnC shown as energy distribution curves (EDCs) (a),(b) and momentum distribution curves (MDCs) (c), (d) along $\Gamma M \Gamma$ (a), (c) (no. 1 in Fig. 3) and $\Gamma K M$ (no. 4 in Fig. 3), respectively.

appears significantly larger than expected near the M point from the k_z projected BS in Fig. 6(a). However, close to E_F (especially the dispersion observed at a larger angle, right of Fig. 5), the observed k_z broadening remains small, leading to well-defined lines. This is in agreement with the quasi-2D character of those bands at E_F. The asymmetry of the ARPES signal intensity between the positive and negative wave-vector area of the spectra is consistent with the asymmetry of the photoionization cross section in s pol mode mentioned above [18].

Other small discrepancies are still found in the area neighboring the boundaries of the BZ for the flatter bands in the -2.0 to -2.5 eV interval. There is a 260 meV downshift between the ARPES and DFT bands near M or K points [see Figs. 5, 6(b), and 7(b)], while the width of the ARPES signal of the bands involved appears to match the broadening of

the DFT bands at or near the BZ edges in Figs. 6 and 7. It must be noted that Sn $p_x + p_y$ orbitals have a more significant contribution to the density of states in this energy range. We performed both SOC and DFT+U calculations with $U = 2$ eV for the p orbital of Sn, but the resulting modifications of the bands were not significant enough to explain the observed relative discrepancies between experiments and calculations at lower energies.

Then, closer to Γ, most of the ARPES bands at -1 eV and below are reproduced quite well by DFT, and the widths of the dispersive features match the ones obtained from the k_z projected band structures in Fig. 7(a). In Figs. 7(b) and 7(c), the band structure is probed over the directions no. 2 and no. 4, which are both equivalent to $K\Gamma K$ but with no. 2 being recorded in a range of θ_y comprising between 25° and 30° and no. 4 for θ_y close to 0°. Comparing the output of Figs. 7(b) and 7(c), the bands that appear on the experimental spectra for the two ΓK directions nos. 2 and 4 are not the same. For no. 2 [Fig. 7(b)], a set of multiple k_z broadened
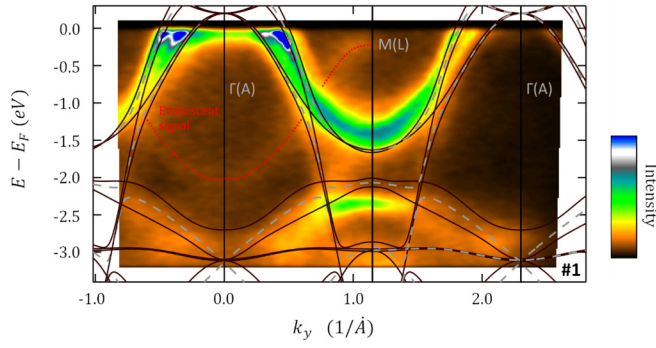
FIG. 5. ARPES BS mapping of a Ti$_2$SnC single crystal oriented over ΓMΓ (respectively *ALA*, and corresponding to no. 1 as above), together with the corresponding bulk bands computed by DFT, in full burgundy lines for ΓMΓ in the Γ plane and dotted gray lines for bands in the *A* planes, along *ALA*. An additional band is featured, whose trace disappears after a few hours and which is not reproduced by bulk DFT calculation (see the dotted red line, used as a guide for the eyes). It shows a minimum at Γ for $E \approx -2.2$ eV. As in all other figures, the color scale is linear.

bands located between Γ and K close to the Fermi level show a higher intensity. These bands are expected to be dominated by d_{xy} and d_{yz} orbitals, which explains why they would have a stronger contribution at high θ_y angles (or high k_y). For no. 4, corresponding to $\theta_y = 0°$, the dispersive features associated with these bands disappear, and the spectrum is dominated by the hexagonal electron tube centered in Γ, which is expected to display a strong d_{z^2} character. The variation of intensity in the ARPES spectra for low and high θ_y angles is thus consistent with the orbital character of the various bands and with the angular dependence of the photoemission cross sections
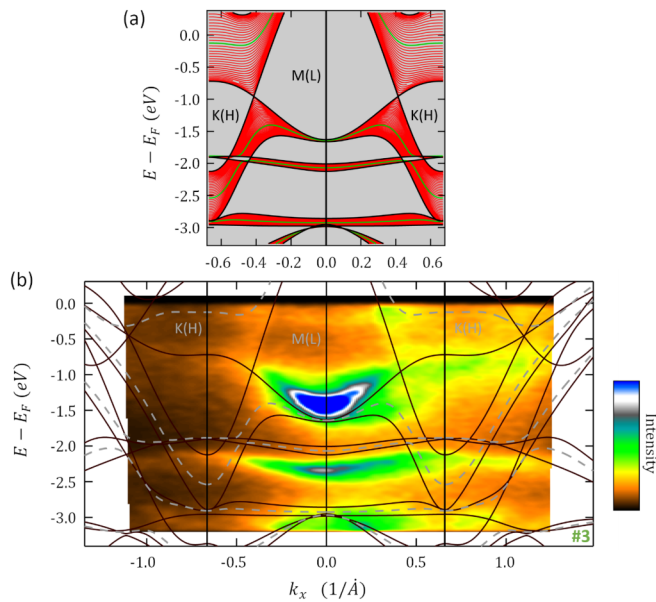
FIG. 6. (a) k_z projected bulk DFT bands over *KMK* (*HLH*) for k_z ranging from 0 (black color) to π/c (green). (b) ARPES band mapping along no. 3, which corresponds to *KMK* (*HLH*) and extends close to Γ(*A*). The color labels of the DFT bands lying either within the Γ or *A* plane correspond to Fig. 5.
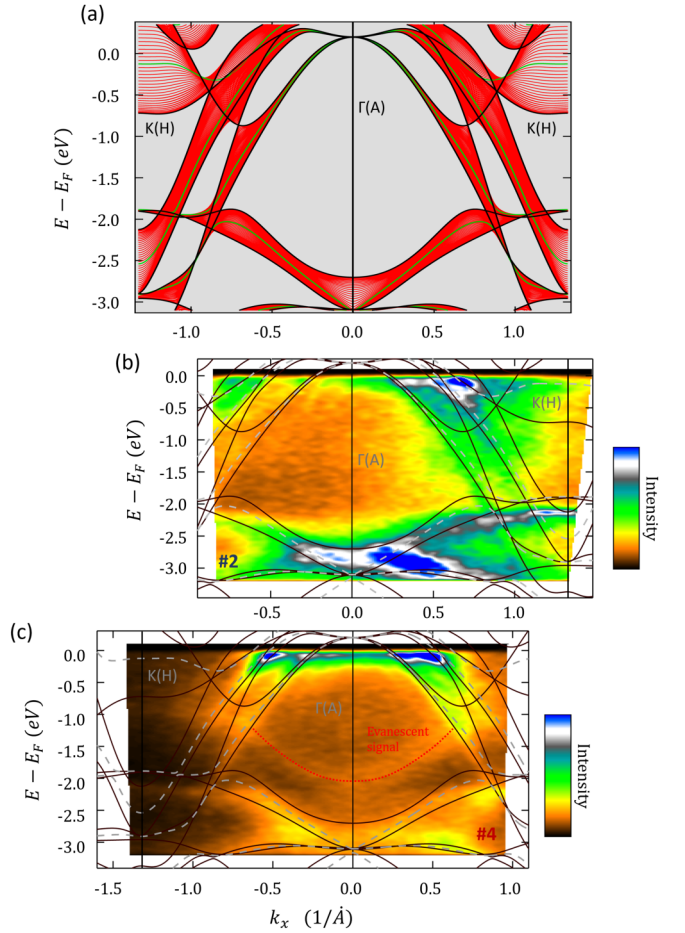
FIG. 7. (a) k_z projected DFT BS along *KΓK*. ARPES spectra along directions no. 2 (b) and no. 4 (c) of Fig. 2. Both spectra account for a band structure along ΓK (*AH*), and they are plotted with corresponding theoretical bands from DFT calculations (in full burgundy for ΓK and dotted gray for *AH*). Part (b) is recorded for relatively large θ_y angles, in a range of 25°–30°, while (c) was recorded at a smaller θ_y value, close to 0°. In (c), the same evanescent dispersions as in Fig. 5 are located near Γ.

computed in [18]. A similar observation stands for the weakly dispersive bands located between –2.0 and –2.5 eV. Overall, it has to be stressed that the agreement between DFT and ARPES is good.

B. Local quasi-2D or quasi-1D dispersions of band 45

Let us first focus on the FS around point H. The latter is exactly centered on the flat FS triangular platelet with a quasi-1D dispersion along the c axis [see Fig. 8(a)]. In Fig. 8(b) are given the dispersion curves parallel to ΓKM, with k_z as a parameter varying across a BZ cut centered on H (the dispersion along *AHL* corresponds to the green line). H, as the other points located midway between the two FS plates, is a quasi-1D Dirac point. It is shown in Fig. 8(c), which displays a 1D Dirac cone along KH. This is also illustrated by the existence of a domain shown in Fig. 8(b) (roughly for $0.5 < k_x < 0.9$ Å^{-1}) for which the in-plane dispersions are almost totally flat regardless of the value of k_z, and the regular spacing between the various k_z values in Fig. 8(b) leads to a
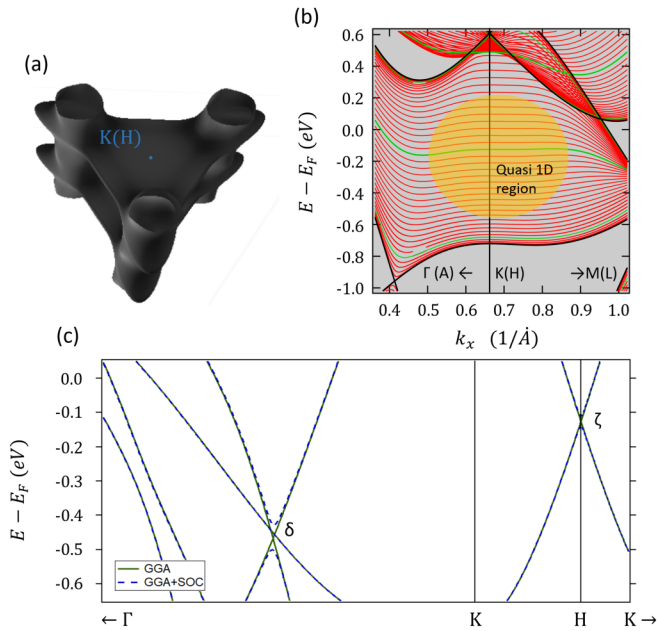
FIG. 8. (a) Electron FS of band 45, which consists of triangular plates centered at the H point and defined in a very narrow window around H. These plates are connected by tubes whose axes are located between Γ and K. (b) Zoom over the k_z-broadened band structure of Ti$_2$SnC near the K point. The dispersion of band 45 is nearly flat around H and for energies close to E_F. (c) Ti$_2$SnC GGA and GGA+SOC band structures along ΓKH. Two linear band crossings are observed at δ and ζ points. Both are gapped when SOC is taken into account, with a gap of roughly 73 meV at δ and 29 meV at ζ.

regular spacing between neighboring dispersion curves. This results from the linear dispersion along k_z. Such a flat dispersion is indeed predicted along any in-plane direction starting from a point located along KH. The quasi-1D Dirac points are located less than 0.1 eV below E_F. When taking SOC into account, a gap opens with a value close to 29 meV [Fig. 8(c)]. Although extracting the dispersion along k_z from the ARPES data would have required detailed measurements and analysis with varying photon energy, a good experimental indication of a dispersive (or not) character along k_z can nevertheless be inferred from observing the ARPES signal intensity and k_z broadening of our spectra acquired for a constant incident photon energy. Roughly speaking, and notwithstanding specific cross-section effects, a band with a strong dispersion along k_z will result in a much weaker signal, dispersed over a wide energy area, whereas a quasi-2D band results, at the 2D limit, in well-defined and thin lines of strong intensity (see, e.g., Ref. [20] for detailed explanations). As shown by Figs. 6(a) and 8(b), the domain around $K(H)$ with a predicted linear dispersion along k_z and no in-plane dispersion does exhibit a low ARPES signal intensity that becomes more intense at its boundaries, where the dispersions are predicted to become 2D and in-plane [Fig. 6(b)]. The same considerations apply to Fig. 7(b). The FS plate corresponding to this quasi-1D linear dispersion should substantially contribute to electrical transport along c.

Let us now consider the FS vertical tubes, the ones intersecting the triangular plates of band 45 at their vertices [see Fig. 8(a)]. From Fig. 9(a), those quasi-2D tubes generate an easily recognizable ARPES signal at E_F, in contrast with the k_z-dispersed triangular plates described just above [the contours of the FSs are also given in Fig. 9(b) for the sake of comparison]. The 2D dispersion of the tubes is also observable in the BS spectra corresponding to cuts nos. 5 and 6 defined in Fig. 2(a). Those spectra are shown in Figs. 9(c) and 9(d). In Fig. 9(d), the 2D-like dispersion displayed by the ARPES signal is clearly parabolic [symmetrical parabola seen at the top left and right of Fig. 9(d)], as predicted by DFT calculations (solid and dashed lines). Those FS tubes should mainly contribute to the in-plane electrical transport, as for other corrugated tubelike FSs with ΓA (bands 39–42) or HK (band 43, tightly enclosing the features of band 45 just described above) as axis.

C. Evanescent surface-state band

Another discrepancy from the predictions of the DFT calculations is the manifestation of an evanescent band in the ARPES spectra of Ti$_2$SnC, with a minimum at Γ and $E - E_F \approx -2.2$ eV, and a maximum near E_F at the M point. This can be observed in Figs. 5 and 7(c). The intensity of this band decreases continuously over time until it almost totally vanishes several hours after the crystals were cleaved in UHV conditions, a fact strongly in favor of a potential surface-state band subject to a slow surface passivation. A similar feature was also observed for V$_2$AlC single crystals [19]. As exposed in [19], it is reasonable to relate this evanescent pattern to the breaking of the d-orbital contribution of the M atom (here Ti), pointing toward the cleaved surface and resulting in the formation of an unstable surface band that follows the original bulk MAX phase hexagonal symmetry. Our data do not allow us to determine the origin of the passivation of the Ti$_2$SnC surface, but a possible explanation may be the oxidation of the upper Ti layer. One can wonder whether such a state would lie at the surface of any MAX phase whose surface has not been reconstructed or oxidized after cleavage. Surface states were not spotted for Cr$_2$AlC and Ti$_3$SiC$_2$ single crystals [18,20], but in these cases they may well have been hidden by the intense signals from the other bulk bands.

V. CONCLUSION AND PROSPECTS

We performed a detailed study of the electronic band structure and Fermi surface of the MAX phase Ti$_2$SnC by means of ARPES and DFT calculations. Following past photoemission studies of MAX phases, we provide an in-depth analysis of the morphology of the FS and of the BS in an intermediate range below the Fermi energy. Ti d orbitals are found to dominate the near E_F electronic structure, while Sn $p_x + p_y$ orbitals become somewhat more prominent at slightly lower energies. The FS is found to be strongly anisotropic and somewhat resembling that of Ti$_3$SiC$_2$. The presence of an additional and evanescent surface-state band is suggested from the comparison between ARPES and DFT band-structure mappings. This work provides a detailed description of the electronic structure of Ti$_2$SnC near E_F and at intermediate en-
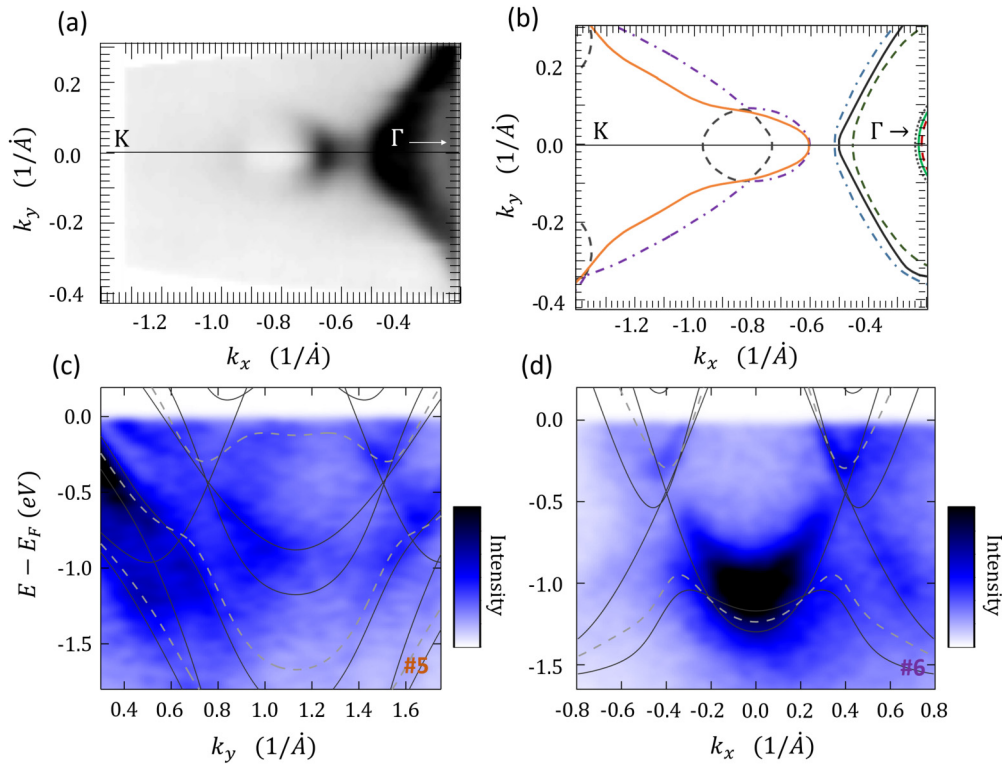
FIG. 9. (a) ARPES mapping of Ti_2SnC Fermi surface (in arbitrary angular units) near δ, close to the center of the two-dimensional tubes joining the triangulate plate of Fig. 8(a). Corresponding DFT Fermi surface cuts are given in (b), where the full and dotted lines stand for the Fermi lines in the *AHL* and the ΓKM planes, respectively. (c) ARPES spectra and DFT bands along no. 5 and (d) along no. 6. Both BSs cross two δ points. Thick darker gray lines stand for the corresponding BS over the Γ plane, and dotted lighter gray lines stand for the *A* plane.

ergies that was still lacking. It may help to further understand the transport properties of this nanolamellar transition metal carbide. The FS is essentially formed of 2D-like tubes (circular or hexagonal) with axis ΓA, 2D-like tubes with *HK* axis (triangular or rounded), and thin plates with a quasi-1D, linear dispersion along c. The triangular tubes closely encircle the complicated band formed by the plates and the small diameter tubes with axis *HK*. It is worth noting that the FS displays a very large number of parallel and flat facets inside the BZ, so that many facets can be obtained from one another by a simple translation with a common translation vector in reciprocal space. This might favor phenomena possibly induced by FS nesting, a point that has not been investigated yet in the case of this particular phase.

In-plane and out-of-plane magnetotransport should therefore display very different properties, with out-of-plane, 1D Dirac electrons and more conventional in-plane hole and electron contributions. To the best of our knowledge, systems combining both kinds of bands (1D and 2D) are seldom found in the literature (see, e.g., Ref. [44]), and they do not exhibit orthogonal 1D and 2D contributions, as should be the case

for Ti_2SnC. A recurrent problem of MAX phase characterization has been the difficulty in assessing magnetotransport anisotropies, due to the lack of thick single-crystal availability [45]. Progress in single-crystal quality should allow one to study that possibility further.

[1] M. W. Barsoum, Prog. Solid State Chem. **28**, 201 (2000).

[2] M. W. Barsoum, *MAX Phases* (Wiley, Weinheim, 2013).

[3] M. Sokol, V. Natu, S. Kota, and M. W. Barsoum, Trends in Chemistry **1**, 210 (2019).

[4] M. Naguib, M. Kurtoglu, V. Presser, J. Lu, J. Niu, M. Heon, L. Hultman, Y. Gogotsi, and M. W. Barsoum, Adv. Mater. **23**, 4248 (2011).

[5] M. Naguib, O. Mashtalir, J. Carle, V. Presser, J. Lu, L. Hultman, Y. Gogotsi, and M. W. Barsoum, ACS Nano **6**, 1322 (2012).

[6] B. Anasori, M. R. Lukatskaya, and Y. Gogotsi, Nat. Rev. Mater. **2**, 16098 (2017).

[7] B. Anasori and Y. Gogotsi, *2D Metal Carbides and Nitrides (MXenes) Structure, Properties and Applications* (Springer International, Cham, 2019).

[8] M. Magnuson and M. Mattesini, Thin Solid Films **621**, 108 (2017).

[9] S. Li, G. Bei, X. Chen, L. Zhang, Y. Zhou, M. Mačković, E. Spiecker, and P. Greil, J. Eur. Ceram. Soc. **36**, 25 (2016).

[10] S. Li, L. Zhang, W. Yu, and Y. Zhou, Ceram. Int. **43**, 6963 (2017).

[11] M. W. Barsoum, G. Yaroschuk, and S. Tyagi, Scr. Mater. **37**, 1583 (1997).

[12] S. Li, G.-P. Bei, H.-X. Zhai, and Y. Zhou, Mater. Lett. **60**, 3530 (2006).

[13] T. El-Raghy, S. Chakraborty, and M. W. Barsoum, J. Eur. Ceram. Soc. **20**, 2619 (2000).

[14] Y. Zhou, H. Dong, X. Wang, and C. Yan, Mater. Res. Innovations **6**, 219 (2002).

[15] H. Högberg, J. Emmerlich, P. Eklund, O. Wilhelmsson, J. P. Palmquist, U. Jansson, and L. Hultman, Adv. Sci. Technol. **45**, 2648 (2006).

[16] M. B. Kanoun, S. Goumri-Said, and A. H. Reshak, Comput. Mater. Sci. **47**, 491 (2009).

[17] Y. C. Zhou, H. Y. Dong, X. H. Wang, and S. Q. Chen, J. Phys.: Condens. Matter **12**, 9617 (2000).

[18] T. Ito, D. Pinek, T. Fujita, M. Nakatake, S. I. Ideta, K. Tanaka, and T. Ouisse, Phys. Rev. B **96**, 195168 (2017).

[19] D. Pinek, T. Ito, M. Ikemoto, M. Nakatake, and T. Ouisse, Phys. Rev. B **98**, 035120 (2018).

[20] D. Pinek, T. Ito, K. Furuta, Y. Kim, M. Ikemoto, S. I. Ideta, K. Tanaka, M. Nakatake, P. Le Fèvre, F. Bertran, and T. Ouisse, Phys. Rev. B **102**, 075111 (2020).

[21] D. Pinek, T. Ito, M. Ikemoto, K. Yaji, M. Nakatake, S. Shin, and T. Ouisse, Phys. Rev. B **100**, 075144 (2019).

[22] Q. Tao, T. Ouisse, D. Pinek, O. Chaix-Pluchery, F. Wilhelm, A. Rogalev, C. Opagiste, L. Jouffret, A. Champagne, J.-C. Charlier, J. Lu, L. Hultman, M. W. Barsoum, and J. Rosen, Phys. Rev. Mater. **2**, 114401 (2018).

[23] M. Barbier, F. Wilhelm, D. Pinek, K. Furuta, T. Ito, Y. Kim, M. Magnier, D. Braithwaite, M. Vališka, C. Opagiste, M. W.

Barsoum, P. Ohresser, E. Otero, P. Le Fèvre, F. Bertran, G. Garbarino, A. Rogalev, and T. Ouisse, Phys. Rev. B **102**, 155121 (2020).

[24] F. Mercier, O. Chaix-Pluchery, T. Ouisse, and D. Chaussende, Appl. Phys. Lett. **98**, 081912 (2011).

[25] T. Ouisse, E. Sarigiannidou, O. Chaix-Pluchery, H. Roussel, B. Doisneau, and D. Chaussende, J. Cryst. Growth **384**, 88 (2013).

[26] L. Shi, T. Ouisse, E. Sarigiannidou, O. Chaix-Pluchery, H. Roussel, D. Chaussende, and B. Hackens, Acta Mater. **83**, 304 (2015).

[27] T. Mitsuhashi, M. Minohara, R. Yukawa, M. Kitamura, K. Horiba, M. Kobayashi, and H. Kumigashira, Phys. Rev. B **94**, 125148 (2016).

[28] A. Damascelli, Z. Hussain, and Z.-X. Shen, Rev. Mod. Phys. **75**, 473 (2003).

[29] P. Blaha, K. Schwarz, F. Tran, R. Laskowski, G. K. H. Madsen, and L. D. Marks, J. Chem. Phys. **152**, 074101 (2020).

[30] J. P. Perdew, K. Burke, and M. Ernzerhof, Phys. Rev. Lett. **77**, 3865 (1996).

[31] M. Kawamura, Comput. Phys. Commun. **239**, 197 (2019).

[32] A. Kokalj, Comput. Mater. Sci. **28**, 155 (2003).

[33] H. Nowotny, H. Boller, and O. Beckmann, J. Solid State Chem. **2**, 462 (1970).

[34] A. Damascelli, Phys. Scr. **T109**, 61 (2004).

[35] S. Moser, J. Electron Spectrosc. Relat. Phenom. **214**, 29 (2017).

[36] S. M. Goldberg, C. Fadley, and S. Kono, J. Electron Spectrosc. Relat. Phenom. **21**, 285 (1981).

[37] A. Bansil, M. Lindroos, S. Sahrakorpi, and R. S. Markiewicz, Phys. Rev. B **71**, 012503 (2005).

[38] M. Lindroos, S. Sahrakorpi, V. Arpiainen, R. S. Markiewicz, and A. Bansil, J. Phys. Chem. Solids **67**, 244 (2006).

[39] J. Krempask'y, V. N. Strocov, P. Blaha, L. Patthey, M. Radovi'c, M. Falub, M. Shi, and K. Hricovini, J. Electron Spectrosc. Relat. Phenom. **181**, 63 (2010).

[40] H. Wadati, T. Yoshida, A. Chikamatsu, H. Kumigashira, H. Eisaki, M. Oshima, Z.-X. Shen, T. Mizokawa, and A. Fujimori, Phase Trans. **79**, 617 (2006).

[41] V. N. Strocov, J. Electron Spectrosc. Relat. Phenom. **130**, 65 (2003).

[42] T. Ouisse and M. W. Barsoum, Mater. Res. Lett. **5**, 365 (2017).

[43] T. Ouisse, D. Pinek, and M. W. Barsoum, Ceram. Int. **45**, 22956 (2019).

[44] H. Jiang, G. Cao, and C. Cao, Sci. Rep. **5**, 16054 (2015).

[45] T. Ouisse, L. Shi, B. A. Piot, B. Hackens, V. Mauchamp, and D. Chaussende, Phys. Rev. B **92**, 045133 (2015).